Design and Evaluation of Pint-Sized Gyroscopic Actuators

1st Cory Meijneke
Electrical and Mechanical Support Div
Delft University of Technology
Delft, The Netherlands
c.meijneke@tudelft.nl

1st Bram Sterke
Department of Rehabilitation Medicine,
Erasmus MC, Rotterdam, NL
Delft University of Technology, Delft, NL
B.T.Sterke@tudelft.nl

2nd Giel Hermans
Electrical and Mechanical Support Div.
Delft University of Technology
Delft, The Netherlands
G.P.Hermans@tudelft.nl

3rd Wouter Gregoor
Electrical and Mechanical Support Div.
Delft University of Technology
Delft, The Netherlands
W.F.Gregoor@tudelft.nl

4th Heike Vallery
Department of BioMech. Engineering,
Delft University of Technology, Delft, NL
Erasmus MC, Rotterdam, NL
h.vallery@tudelft.nl

5th Daniel Lemus
Department of Rehabilitation Medicine,
Erasmus MC, Rotterdam, NL
Delft University of Technology, Delft, NL
d.lemusperez@erasmusmc.nl

Abstract—One important aspect of gait stability is the control of whole-body centroidal angular momentum H. We recently showed that if sensory-motor impairments affect a person's balance control, control of H can be assisted by control moment gyroscopes (CMGs). However, the effect of CMG technology inherently depends on the size and weight of these actuators, and on the speed of the flywheels they contain. These factors all pose challenges for wearable applications. Here, we show that it is possible to design CMGs light enough for wearable applications, while generating meaningful output torques. Our CMG, weighing $1.187\,\text{kg}$, can exert a peak torque of $15\,\text{N}\,\text{m}$ with a torque-tracking bandwidth of $18\,\text{Hz}$. These results are partly due to an integrated model of components and partly to advancements in flywheel velocity control, allowing the speed to safely reach $20\,000\,\text{rpm}$. These actuators open up new pathways of building wearable assistive devices for clinical applications.

Index Terms—control moment gyroscope, CMG, flywheel speed, assistive device.

I. INTRODUCTION

In our rapidly aging societies, age-related motor impairments generate an increasing strain on health care systems. Morbidity caused by falling strongly contributes to this strain [1]. Falling is positively correlated with age [2], as aging is accompanied by a decrease in gait stability [3].

One important aspect of gait stability is the control of centroidal angular momentum H [4]. Modifying H requires external forces or moments, but these are difficult to generate with wearable technology. One possible solution is the use of angular momentum exchange devices, commonly containing one or more flywheels. Such devices can generate moments without anchoring to an inertial frame, making them excellent candidates for wearable devices that influence H [5].

Angular momentum can for example be exchanged by the reaction wheel effect [6] or by letting gyroscopic moments be induced by rotational motion of human body segments. Self-induced moments tend to reduce this human motion, for example damping tremor of Parkinson patients [7]. A

third, highly controllable way of angular momentum exchange is given by single-gimbal or dual-gimbal control moment gyroscopes (CMGs) [8]–[10]. Fig. 1 depicts a single-gimbal control moment gyroscope (SGCMG), which comprises a fast-spinning flywheel enclosed in an inner gimbal frame, which is in turn rotated or *gimbaled* by a gimbal motor located in the outer gimbal frame.

CMG technology has been applied predominantly in space, to control orientation of satellites or even of the ISS space
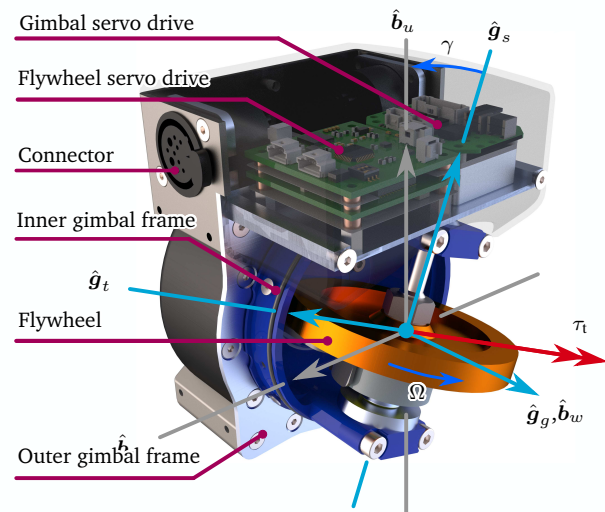

Fig. 1: Overview of the CMG's main components with flywheel cover removed. The respective frames $\mathcal{G} = \{\hat{\boldsymbol{g}}_s, \hat{\boldsymbol{g}}_t, \hat{\boldsymbol{g}}_g\}$ and $\mathcal{B} = \{\hat{\boldsymbol{b}}_u, \hat{\boldsymbol{b}}_v, \hat{\boldsymbol{b}}_w\}$ denote the inner and outer gimbal reference frames. The flywheel spins at an angular rate Ω and rotates about the gimbal axis $\hat{\boldsymbol{g}}_g$ at a rate $\dot{\gamma}$, generating a gyroscopic torque τ_t about the mutually orthogonal axis $\hat{\boldsymbol{g}}_t$.

station [9]. However, new research mostly focuses on very small devices, as needed for nano-satellites.

Few attempts at wearable CMGs have been published. After a first simulation [11], we realized a CMG with peak output torque of 70 N m at a total mass of approximately 10 kg [12]. Others have realized wearable scissored-pair CMGs (SPCMG) with masses between 8 kg to 20 kg mass and torque outputs of 6 N m to 20 N m [8], [13]. Placing CMGs on other parts of the body has been explored for space applications[14].

Recently, we showed that SGCMGs located on the trunk can improve human dynamic balance. In that study, the CMG exerted peak moments in the order of 15 N m during all experiments [15]. One major challenge, however, is reducing device size and weight in order to meet usability requirement imposed by the physical strength of the target population [15].

In this paper, we propose CMGs that can be worn in a modular way, at different locations of the body, such as trunk and leg. We drastically reduced target mass to less than 1.5 kg for one CMG, while simultaneously reducing the allowed envelope and keeping the target torque output in the same order of magnitude. As a result of the CMG's working principle, the reduction of mass and size had to coincide with an ambitious increase in the flywheel speed, to 20 krpm. To reach these targets, we used a multi-physics simulation considering the complex interplay between the various physical effects. For example, this comprehensive model takes into account how flywheel aerodynamics influence motor temperature, or how bearing friction depends on gyroscopically induced loads in response to a wearer's motion.

The design resulted in a gyroscopic actuator with dimensions of 101 mm × 92 mm × 117 mm and mass of 1.2 kg.

The following sections cover the CMG working principle, user requirements, simulation and hardware design, control design, and experimental evaluation.

II. Hardware Design

A. Working principle and requirements

A CMG exerts gyroscopic torques due to the change in direction of the angular momentum vector $\boldsymbol{H}$ of the flywheel. This angular momentum vector is a function of flywheel inertia J_{Ws} and flywheel speed Ω, and it points in direction of the spinning axis $\hat{\boldsymbol{g}}_s$: $\boldsymbol{H} = J_{Ws}\Omega\hat{\boldsymbol{g}}_s$. To accomplish a gyroscopic effect, the inner gimbal frame $\mathcal{G}$ rotates the spinning flywheel around a perpendicular axis $\hat{\boldsymbol{g}}_g$ at an angular velocity $\dot{\gamma}$ (Fig. 1). The main generated gyroscopic torque τ_t about the $\hat{\boldsymbol{g}}_t$-axis can be approximated as [16]:

$$\tau_t \approx -J_{Ws}\Omega(\dot{\gamma} + \boldsymbol{\omega}^T\hat{\boldsymbol{g}}_g). \tag{1}$$

Similarly, the two torques τ_s and τ_g about the flywheel axis $\hat{\boldsymbol{g}}_s$ and the gimbal axis $\hat{\boldsymbol{g}}_g$, are approximated as:

$$\tau_s \approx J_{Ws}\dot{\gamma}\boldsymbol{\omega}^T\hat{\boldsymbol{g}}_t + J_{Ws}\dot{\Omega} \tag{2}$$

$$\tau_g \approx -J_{Ws}\Omega\boldsymbol{\omega}^T\hat{\boldsymbol{g}}_t + J_{Wg}\ddot{\gamma} \tag{3}$$

Note that disturbance torques are present if an angular velocity $\boldsymbol{\omega}$ is imposed on the CMG's outer gimbal frame by the

movement of the human body, i.e. the $\mathcal{B}$-frame. The torques to the user τ_u, τ_v and τ_w in the $\mathcal{B}$-frame consist of desired, effective, components and undesired components, which are not aligned with the reference torque vector. The user-imposed motion $\boldsymbol{\omega}$ and the effective torque component(s) depend on the application.

Our primary design goal was to apply moments to a humans body part, e.g. trunk or leg, during walking. (Fig. 2). The target requirements (see Table I) for the design of the CMG originated from the extreme case of attaching the device to the human leg and applying shorts bursts of torque to augment the wearer's leg movement (see Fig. 2). Then the gyroscopic disturbance torques, as seen from Eq. (3) will be high due to the high angular velocity of the leg. In the lower leg, the device mass is also very critical.

The self-induced gimbal disturbance torque can make it difficult for the gimbal motor to track a given velocity profile, as needed to induce desired gyroscopic moments (Eq. (1)). The requirements considered the angular velocity of the thigh during regular walking [17] as disturbance $\boldsymbol{\omega}$. The torque and time requirements in Table I are defined in the effective direction, which for this application is the $\hat{\boldsymbol{b}}_v$-axis.
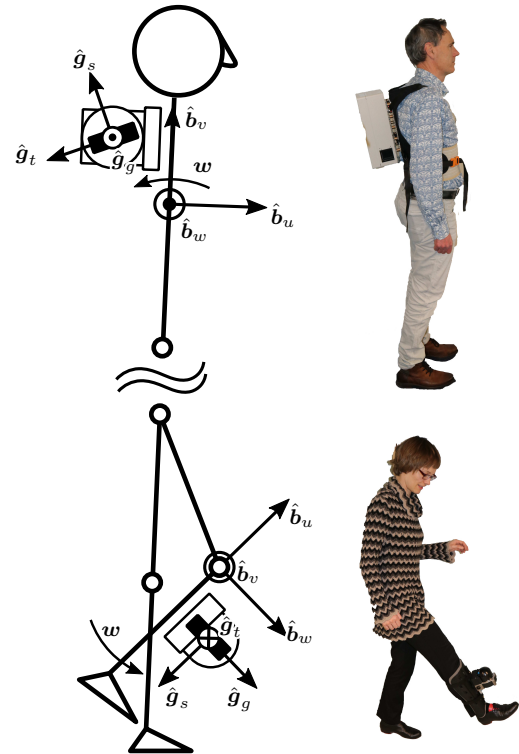

Fig. 2: Two alternative example applications of the CMG in human locomotion. Each CMG can be oriented in three orientations. The figures with the humans show the currently described CMG on the leg and show a backpack configuration that contains two CMGs.
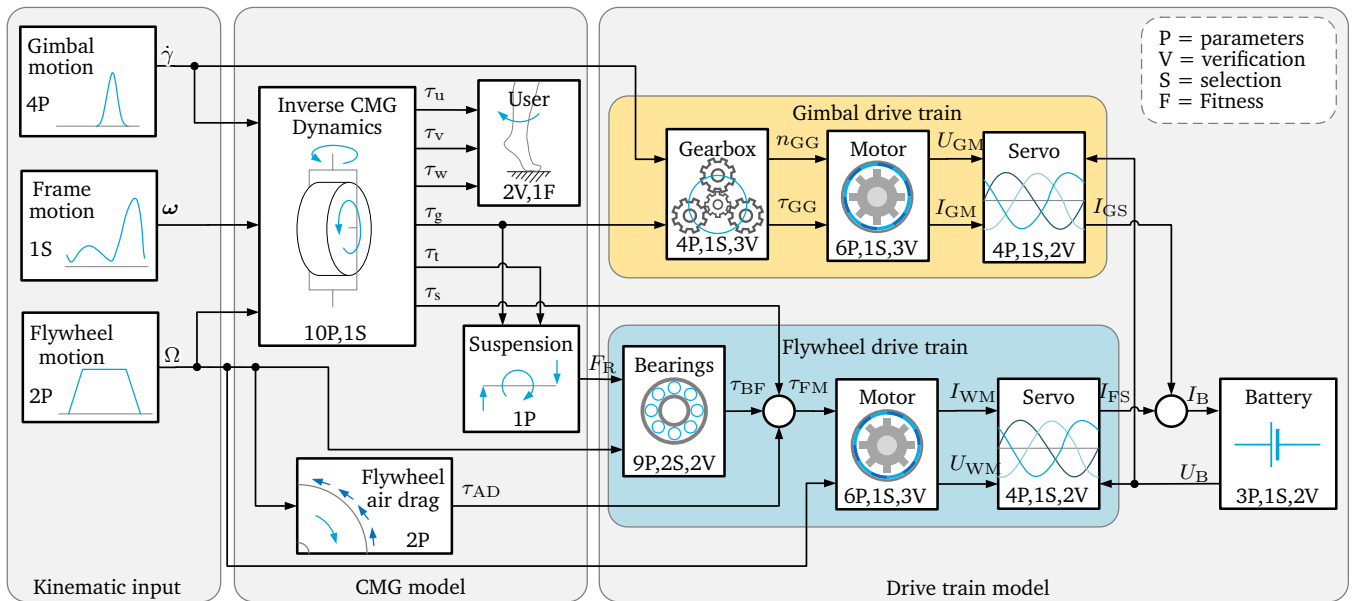
Fig. 3: Simulation model of the CMG including the drive trains. Kinematic inputs include the desired gimbal motion $\dot{\gamma}$ the desired flywheel motion Ω, environment disturbance motion $\boldsymbol{\omega}$,. The CMG model includes the torque components (τ_s, τ_g, τ_t), radial bearing load F_R, air drag τ_{AD}, and torques on the outer gimbal frame (τ_u, τ_v, τ_w) provided to the user. The flywheel drive train includes the bearing friction τ_{BF}, the total force on the motor τ_{FM}, the motor current I_{WM} and voltage U_{WM}, and servo drive current I_{WS}. The gimbal drive train includes the gearbox input speed n_{GM} and moment τ_{GM}, the motor current I_{GM} and voltage U_{GM}, and the servo drive current I_{GS}. The battery model includes the voltage U_B and the total current I_B. Each block denotes the number of inputs (parameters (P) and selected component (S)) and outputs (verification checks (V) and fitness (F)) (excl. universal constants)

B. Simulation Model

In designing a complex system like the CMG within strict constraints and with ambitious performance targets, we took guidance from a simulation model (see Fig. 3). In addition to predicting the gyroscopic torques, this model also included detailed engineering calculations to do verification-checks on all of its components (i.e. motors, gears, bearings, etc.). This requires a multi-physics simulation that includes models of tribology, rigid body dynamics, fluid dynamics, and electrical domain. The model captures the interplay between components and aids in balancing components performance and mass with respect to each other. The model cannot predict the implications of component placement in the design space, hence it was used in collaboration with CAD design. Additionally, finite element analysis (FEM) was used to analyze detailed material-stresses. The simulation investigates feasibility of accelerations and power that are required to track kinematic input, but it does not include closed-loop behaviour. It does provide the set-points, such as Ω_{ref}, and constraint checks, such as $\ddot{\gamma}_{max}$,

to the control model, detailed in Fig. 4. The main targets of the simulation were; minimizing power consumption and component weight, while maximizing the effective torque τ_u generated in $0.1\,\mathrm{s}$.

The interplay between the components and the constraints is exemplified by the flywheel bearing selection. To allow higher moments to be generated, it is possible to increase the flywheel bearing size. However, increasing the bearing size also increases the bearing friction, whereby reducing the attainable flywheel speed, resulting in a decreased generated moment. Subsequently increasing flywheel motor size to overcome the reduction in flywheel speed would result in increased size, mass, and power consumption.

At the core of the simulation is an inverse-dynamics model of the flywheel, described in section Section II-A. The kinematic inputs depend on the specific application. Here, the motion $\boldsymbol{\omega}$ of the $\mathcal{B}$-frame represents physiological thigh motion during locomotion [17]. The outputs are actuator torques and moments acting on the user. Wheel model parameters are material and dimensions of the flywheel. The CMG model further includes flywheel air drag [12] and it converts the gyroscopic moments to radial bearing loads, as needed in the second layer to predict friction in the wheel bearing suspension.

The second layer of the model describes the drive trains for gimbal and flywheel. Each part of the model only contains the components that are critical to the device performance. To

TABLE I: Target requirements for the CMG

Target requirement	Value	Unit
Target pulse gyroscopic torque	15	N m
Target pulse time	0.1	s
Max actuator weight	1.5	kg

estimate bearing friction, we used the SKF bearing friction model [18]. The calculations for a (generic) gearbox, motor and servo drive are according to [19]. The parameters in the drive train models are driven by data sheets of suppliers. The simple battery model predicts battery weight and size for the application given the desired battery life.

C. Component design

The CMG consists of a flywheel, suspended in the inner gimbal frame, which – in its turn – is suspended in the outer gimbal frame (Fig. 1).

1) The outer gimbal frame: consists of a titanium grade 5 3D-printed component with several bolt hole arrays. Therefore, the device can be mounted in different orientations.

2) The inner gimbal: is suspended in a large thin-section X-bearing (Kaydon KA025KP0), allowing it to rotate about the $\hat{g}_g$-axis. A large outrunner brushless motor is used (T-motor U8 Lite, Kv85). The motor encloses a position encoder (RLS AksIM-2, 19 bit BiSS) and a slipring (Gileon SRC012-12) to power the flywheel motor while allowing for continuous gimbal rotation. Before choosing the direct-drive option for gimbal actuation, a worm-gear, harmonic-drive and belt drive were considered. The behaviour and constraints of those option were inserted in the gearbox block in Fig. 3 (the simulation), which quickly showed some insurmountable limitations (e.g. with the viable gearbox ratios of those solutions and the required output accelerations, the reflected inertia becomes a problem). To drive the motor, we chose the Ingenia Everest XCR servo drive, for its high power output, small lightweight footprint, and CiA 402 EtherCAT compliance.

3) The flywheel: is fabricated from Densimet (Plansee, D170), which has a high density ($17.5\,\mathrm{g/cm^3}$). After obtaining the overall dimensions from from the multi-physcs simulation, the challenge was to implement the flywheel such that it could withstand the centrifugal and gyroscopic loads with minimal use of material. The flywheel integrity was verified by simulations performed in ANSYS Workbench 2019. The shape was iteratively determined such that the design yield stress is not exceeded and cyclic stress contributing to fatigue (caused by gyroscopic torque) does not exceed the design fatigue limit. This resulted in a flywheel with an inertia J_{Ws} of $2.265 \times 10^{-4}\,\mathrm{kg\,m^2}$. The flywheel is suspended within the gimbal frame by two bearings (SKF 604-2Z), and it is powered by a small brushless outrunner motor (T-Motor F60-PRO). The target speed for the flywheel is $20\,\mathrm{krpm}$, which corresponds to an angular velocity of $\Omega = 2094.4\,\mathrm{rad/s}$ resulting in an angular momentum H of $0.474\,\mathrm{N\,m\,s}$.

The flywheel motor drive is an in-house development based on InstaSPIN FOC from Texas Instruments (TI). The reason for this choice is the combination of sensorless motor control, high velocity, low motor inductance, and high ratio of load inertia to motor inertia, making it difficult to use a commercially available drive.

III. Control

A. CMG torque control

As is common for CMG, torque is indirectly controlled via gimbal velocity. Using Eq. (1), the torque controller of the CMG generates a desired gimbal frame velocity $\dot{\gamma}_{\mathrm{ref}}$ in an open-loop fashion, as seen in Fig. 4. To monitor the generated torque, we also estimated the generated output torque by the same approximated dynamics of Eq. (1).

We used the built-in velocity control mode of the gimbal servo drive for velocity tracking, given its ten times faster feedback loop of $100\,\mu\mathrm{s}$ compared to the EtherCat master controller, and the added advantage of decentralizing computational load.

An indirect feed-forward friction compensator (IFFC) further improves control performance, by taking advantage of knowing the reference gimbal velocity, This was only possible indirectly, because the gimbal drive does not accept a feed-forward torque input. However, we implemented such feed-forward by using the P-gain $k_{p,\mathrm{XCR}}$ of the drive only, and superimposing scaled feed-forward onto the reference velocity, which thereby doubles as a carrier (Fig. 4) .

TABLE II: CMG control parameters

Parameter	Symbol	Value	Unit
CMG torque control			
Sampling rate	f_{s}	1000	Hz
Max allowable torque output	τ_{max}	20	N m
Feed-forward friction compensation			
Viscous friction coefficient	k_v	0.012	A s/rad
Coulomb friction coefficient	τ_C	0.818	A
Drive velocity control			
Flywheel			
Max allowed angular velocity	Ω_{ref}	20 000	rpm
Gimbal			
Closed loop sample rate		10 000	Hz
Velocity proportional gain	$k_{p,\mathrm{XCR}}$	20	A s/rev
Max allowed angular velocity	$\dot{\gamma}_{\mathrm{max}}$	6.7	rev/s
Max allowed angular acceleration	$\ddot{\gamma}_{\mathrm{max}}$	20	rev/s^2

B. Flywheel control

The permanent-magnet synchronous motor (PMSM) was chosen based on performance and mechanical integration. Although brush-less DC motors are conventionally more advantageous to PMSM motors at high velocities; in our case the lower torque-ripple of the PMSM type is advantageous as it produces lower noise and vibrations, which in wearable applications is important. The trade-off is that PMSM requires a more complex controller that can generate a proper 3-phase sinusoidal excitation at the requested frequency.

The current type of motor is typically not designed for applications with such high inertia load. Control of flywheels with such high load to rotor inertia ratio conventionally requires a position sensor to reliability start the motor, to overcome commutation issues. Position sensors were incompatible with the tight volume and mass constraints. Adding a torque feed-forward to the velocity control loop, increasing torque at low Ω, solved this problem.
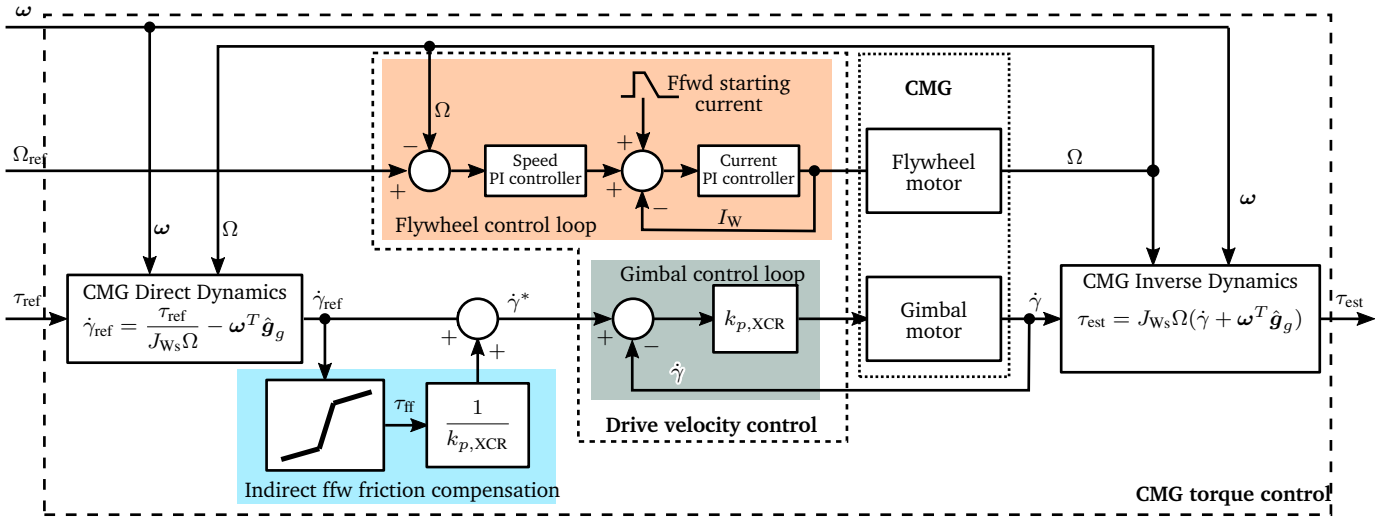
457

Fig. 4: CMG control block diagram showing the cascaded controller. Torque control is implemented in the EtherCAT master, while the velocity controllers are implemented in the flywheel and gimbal motor drives.

For PMSM motors a field-oriented control (FOC) is most suitable [20]. We used a FOC-based motor controller from Texas Instruments (TI), InstaSPIN FOC. Settings of pulse width modulation (PWM) frequencies and velocity and current loop frequencies were tuned to deal with the low motor inductance and high velocities. Analysis of the power dissipation at various PWM frequencies provided the PWM frequency choice of $60\,\mathrm{kHz}$.

IV. EVALUATION SETUP AND PROTOCOL

A. Experimental setup

In the experimental setup (see Fig. 5), the CMG was attached to a calibrated six-axes multi-component sensor (K-MCS10-010-6C, HBM GmBH). IgH Test Manager was used for monitoring, manipulation of the control parameters and for logging data. The CMG control parameters can be found in Table II. The device was powered by a power supply connected to mains.

B. Torque tracking and disturbance rejection protocols

To evaluate torque tracking performance and bandwidth of the CMG, we used a multisine as reference input speed $\dot{\gamma}_{\mathrm{ref}}$. Frequencies ranged from $0.05\,\mathrm{Hz}$ to $50\,\mathrm{Hz}$.

We chose the amplitude such that the gimbal acceleration remained below its maximum at high frequencies. Two oscillations were applied per frequency.

To evaluate how timely the torques can assist users, we used reference block pulses of multiple durations ($1\,\mathrm{N\,m}$ to $15\,\mathrm{N\,m}$) and magnitudes ($2\,\mathrm{Hz}$ to $20\,\mathrm{Hz}$) as input.

To evaluate tolerance to disturbance body angular velocity $\boldsymbol{\omega}$, we set the gimbal to position control, manually applied torques to it, and recorded resulting changes in angle (position control was used here because velocity control allows the position to drift). Using Eq. (1), the maximally held torque
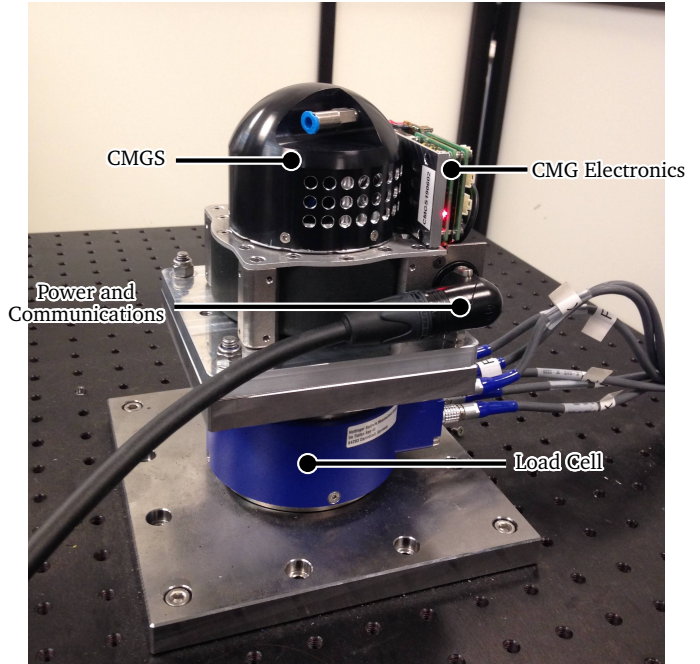

Fig. 5: The control moment gyroscope is located on top of a 6D Multicomponent Sensor (HBM, Darmstadt GE)

before giving way can be directly translated to the maximally supported $\boldsymbol{\omega}$.

C. Signal processing

We recorded estimated gyroscopic output torque and load-cell readings. The estimated torque was calculated using Eq. (1). The load cell horizontal torque components were mapped via the rotation matrix, which is a function of γ, to obtain the gyroscopic torque in the rotating $\hat{\boldsymbol{g}}_t$-direction. For

the multisine, we extracted the sampled frequency response by fitting a sine to the second cycle of the output at each frequency.

For visual analysis in plots, we removed high-frequent signal components from the raw recorded load cell data. We set a cut-off frequency of 50 Hz for the subsequent 2nd-order Butterworth filtering (applied forward and backward to the offline data, to avoid phase delay). For the identification of the frequency response, we used the raw, unfiltered data. The analysis was implemented using MATLAB®.

V. RESULTS

A. Flywheel performance

We observed a theoretically possible flywheel speed of up to approximately 24 krpm. However, as all FEM simulations and safety factors were made for 20 krpm only, we chose a peak flywheel speed of 20 krpm for all experiments. The flywheel has a 50% and 100% rise time of respectively 107 s and 211 s to maximum velocity. The supply power at 20 krpm is 22.2 W, while at 10 krpm it is approximately 8 W.

B. Torque tracking and disturbance performance

Fig. 6 shows reference torques and corresponding estimated and actual torques for 1 Hz, 10 Hz, 18 Hz, and 30 Hz. The estimated torque is based on Eq. (1) and the actual $\dot{\gamma}$. The frequency response (Fig. 7) shows a magnitude drop of -2 dB at 18 Hz. After 18 Hz non-linear effects start to occur; possibly due to resonance of the load-cell.

Fig. 8 displays the results of the torque pulse test at 5 Hz. The delay between pulse onset and when the measured torque reaches the threshold, calculated for 15 N m, was 15 ms. The torque components τ_u and τ_v are measured by the load cell, in the table-fixed directions $\hat{u}_u$ and $\hat{u}_v$ respectively. This shows the desired torque τ_u and undesired, non-aligned, torque τ_v. In a SPCMG the non-aligned torques cancel each-other, leaving only $\hat{u}_u$.

During the disturbance evaluation the gimbal was able to hold torques of up to 2.3 Nm. Using Eq. (1), with $\dot{\gamma} = 0$, this indicates that the CMG can withstand disturbances in body angular velocity of up to 4.8 rad/s.

VI. DISCUSSION

A. Actuator performance

The torque tracking performance of the CMG exceeds the bandwidth requirements of the application. Human movement, particularly of the whole body, does not exhibit higher components than about 5 Hz, which is low compared to the 18 Hz of the designed actuator. The low friction and the good torque tracking confirm the expected benefits of the hardware selection, in particular the direct drive.

A limitation of the experimental evaluation is that the table-mounted configuration does not allow investigating the influence of human motion on the system, besides the manual application of torques in the experiments. In a wearable application, the angular velocity ω of the $\mathcal{U}$-frame generates moments which need to be overcome by the gimbal motor.
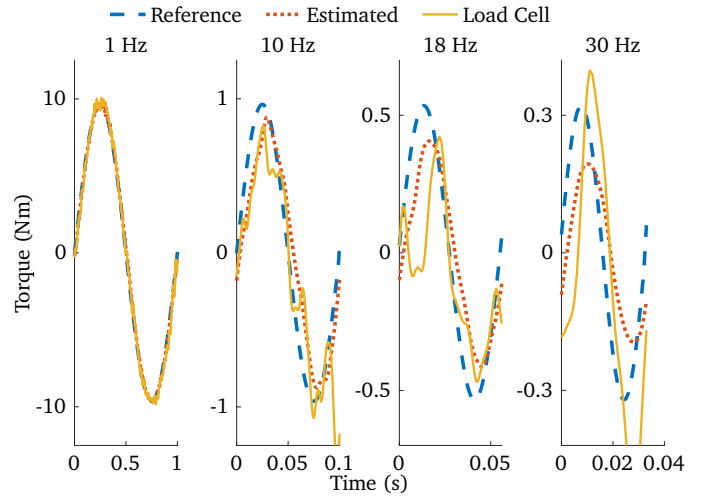

Fig. 6: Reference, estimated, and load cell torque for 1 Hz, 10 Hz, 18 Hz and 30 Hz, showing tracking performance.
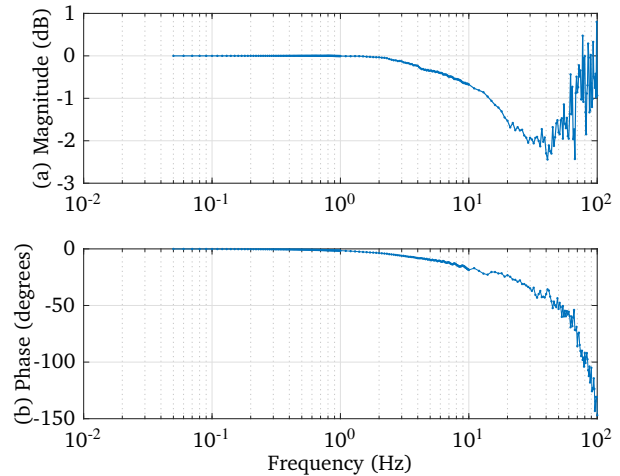

Fig. 7: Frequency response of the CMG, showing the drop in magnitude (in dB) and the phase shift (in degrees) of the output torque with respect to a multisine reference.

In practice, this is expected to affect both model-based torque estimation and velocity tracking performance.

B. Implications for the wearable application

The main advantage of wearable control moment gyroscopes is that they impart moments onto a body without the need of anchoring to an inertial frame, e.g. the floor or a wall. Until now, the mass of the technology has been the main limiting factor in the application for clinical use.

Promisingly, with a mass of around 1.2 kg, a maximum peak torque of 15 N m and a torque-to-mass ratio of 12.6 N m/kg, our CMG has entered the range of other wearable assistive devices, see Table III. The preliminary backpack configuration used in the comparison contains the harness, two CMGs, a fan,
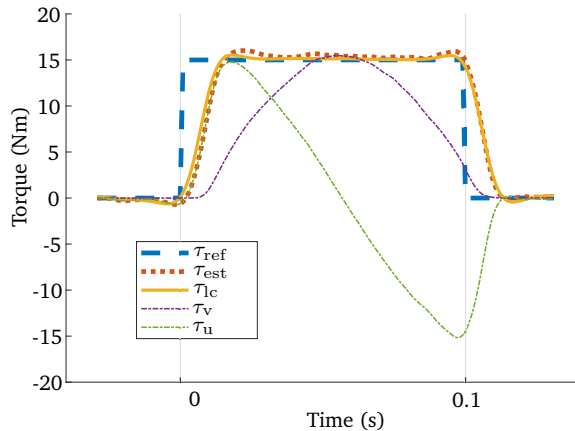
Fig. 8: Exemplary torque pulse test, showing the $15\,\mathrm{N\,m}$ reference τ_ref, estimated τ_est, and load cell torque τ_lc corresponding to $10\,\mathrm{Hz}$. Components τ_u and τ_v of the load cell torque are expressed in the $\mathcal{B}$-frame.

a PCB and wiring. Likewise our device is outperforming the top nano-satellite CMG reported by Gaude and Lappas [21], which shows a torque/mass ratio of 0.29. The latter is clearly designed to meet very different requirements and environments; this emphasizes the need for a design for terrestrial applications.

TABLE III: Comparable devices

Authors	Mass (kg)	Torque/mass ratio (N m/kg)
Current paper (CMG only)°	1.19	12.6
Current paper (Backpack)△	5.13[1]	5.8
Romtrairat et al. [8] △	15.03	0.4
Lemus et al. [12] °	10	7.0
Chiu and Goswami [13] △	6.7[2]	3.0
Chinimilli et al. [22] ×	1.57	7.2
Beusing et al. [23] ×	1.1[3]	5.5

° single CMG   △ scissored paired CMG   × Exoskeleton
[1] excluding battery and control
[2] after subtracting 1 kg for the battery.
[3] after subtracting 0.6 kg for the battery and dividing by two for each leg.

One remaining challenge is the vibration and noise that are generated when the flywheel is at maximum velocity. As the connection in the eventual application consists of textile and cushioning, the vibration will most likely be dissipated more than by our current table mount. We also hope to address noise by further reducing resonating structures and creating an isolated casing.

Any CMG can only handle short bursts or mean-free cyclical moment tracking tasks. That is due to its operating principle, which is subject to singularities. Therefore, it is not possible to generate a continuous torque, for example to counteract gravitational moments. We showed in the past that

singularities can be dealt with without adverse effects such as oscillations [5], [24], and balance assistance with CMGs can be effective [15] despite its limitation to mean-free assistance.

Moving towards an untethered assistive device, the CMG has to be battery-powered. During the multi-sine tests (a worst-case situation), the gimbal motor drew an RMS current of $1.7\,\mathrm{A}$ at $12\,\mathrm{V}$, which equates to approximately $21\,\mathrm{W}$. With an additional $22.2\,\mathrm{W}$ for the flywheel when running at $20\,\mathrm{krpm}$, the total power consumption is $43.2\,\mathrm{W}$. Thus, using 2x3 $3.6\,\mathrm{V}$ Lithium cells with $2550\,\mathrm{mAh}$ capacity and a 20% rated discharge margin would give an effective total discharge capacity of $44\,\mathrm{Wh}$. This could power the device for about an hour. At a mass of $0.28\,\mathrm{kg}$, this battery provides a meaningful duration for a therapy session or a walk through the park.

The developed pint-sized CMGs could be attached to diverse body parts. However, their potential for specific applications remains to be scrutinized. For example, simulations indicated that CMGs hold promise for increasing step length, but exoskeletons outperform them in increasing toe clearance [25]. It would also be interesting to compare angular momentum exchange to linear momentum exchange devices like cold gas thrusters [26].

C. Future work

To advance towards clinical application of CMGs, future work will focus on combining multiple CMGs, which enables torques over multiple axes and compensation of parasitic moments. In parallel, we are investigating specific clinical use-cases and high-level control paradigms. To ensure safety during use on humans, endurance and reliability tests are being performed, prior to a planned pilot on able-bodied subjects.

VII. Conclusion

We presented a gyroscopic actuator with dimensions of $101\,\mathrm{mm} \times 92\,\mathrm{mm} \times 117\,\mathrm{mm}$ and mass of $1.2\,\mathrm{kg}$, capable of producing block torque pulses of $15\,\mathrm{Nm}$ for $0.1\,\mathrm{s}$.

This shows that it is possible to realize terrestrial-application CMGs with superior torque-to-weight ratio, making it now conceivable to use such actuation technology for wearable balance-augmenting devices.

The design method was based on a multi-physics simulation model, containing rigid body dynamics, fluid dynamics, tribology, and electrical domain modeling linked with other hardware design tools like FEM, enabling iterative choice and tuning of individual components.

460

Supplementary Materials

In order to allow verification and review of our data and script, we have uploaded the resources to an open-access public repository available in the 4TU.ResearchData [27].

References

[1] L. Z. Rubenstein, "Falls in older people: Epidemiology, risk factors and strategies for prevention," *Age and Ageing*, vol. 35, no. suppl_2, pp. ii37–ii41, Sep. 2006.

[2] M. Tieland, I. Trouwborst, and B. C. Clark, "Skeletal muscle performance and ageing," *Journal of Cachexia, Sarcopenia and Muscle*, vol. 9, no. 1, pp. 3–19, 2018.

[3] S. M. Bruijn, O. G. Meijer, P. J. Beek, and J. H. v. Dieën, "Assessing the stability of human locomotion: A review of current measures," *Journal of The Royal Society Interface*, vol. 10, no. 83, p. 20 120 999, Jun. 2013.

[4] C. R. Nott, R. R. Neptune, and S. A. Kautz, "Relationships between frontal-plane angular momentum and clinical balance measures during post-stroke hemiparetic walking," *Gait & Posture*, vol. 39, no. 1, pp. 129–134, Jan. 2014.

[5] A. Berry, D. Lemus, R. Babuska, and H. Vallery, "Directional Singularity-Robust Torque Control for Gyroscopic Actuators," *IEEE/ASME Transactions on Mechatronics*, vol. 21, no. 6, pp. 2755–2763, Dec. 2016.

[6] T. Wojtara, M. Sasaki, H. Konosu, M. Yamashita, S. Shimoda, F. Alnajjar, and H. Kimura, "Artificial balancer – Supporting device for postural reflex," *Gait & Posture*, vol. 35, no. 2, pp. 316–321, Feb. 2012.

[7] A. S. Wehse, D. Muse, and I. Sun, "Gyroscopic Stabilization for Uniaxial Hand Tremors," Worcester Polytechnic Institute, Tech. Rep., 2019.

[8] P. Romtrairat, C. Virulsri, P. Wattanasiri, and P. Tangpornprasert, "A performance study of a wearable balance assistance device consisting of scissored-pair control moment gyroscopes and a two-axis inclination sensor," *Journal of Biomechanics*, vol. 109, p. 109 957, Aug. 2020.

[9] C. Gurrisi, R. Seidel, S. Dickerson, S. Didziulis, P. Frantz, and K. Ferguson, "Space station control moment gyroscope lessons learned," *Proceedings of the 40th Aerospace Mechanisms Symposium*, vol. NASA/CP-2010-216272, pp. 161–176, 2010.

[10] F. Y. Toriumi and B. A. Angelico, "Nonlinear Controller Design for Tracking Task of a Control Moment Gyroscope Actuator," *IEEE/ASME Transactions on Mechatronics*, vol. 25, no. 1, pp. 438–448, Feb. 2020.

[11] D. Li and H. Vallery, "Gyroscopic assistance for human balance," in *2012 12th IEEE International Workshop on Advanced Motion Control (AMC)*, Sarajevo, Bosnia and Herzegovina: IEEE, Mar. 2012, pp. 1–6.

[12] D. Lemus, J. van Frankenhuyzen, and H. Vallery, "Design and Evaluation of a Balance Assistance Control Moment Gyroscope," *Journal of Mechanisms and Robotics*, vol. 9, no. 5, Aug. 2017.

[13] J. Chiu and A. Goswami, "Design of a Wearable Scissored-Pair Control Moment Gyroscope (SP-CMG) for Human Balance Assist," *Proceedings of the ASME 2014 IDETC/CIE 2014*, Aug. 2014.

[14] K. R. Duda, R. A. Vasquez, A. J. Middleton, M. L. Hansberry, D. J. Newman, S. E. Jacobs, and J. J. West, "The Variable Vector Countermeasure Suit (V2Suit) for space habitation and exploration," *Frontiers in Systems Neuroscience*, vol. 9, Apr. 2015.

[15] D. Lemus, A. Berry, S. Jabeen, C. Jayaraman, K. Hohl, F. C. T. van der Helm, A. Jayaraman, and H. Vallery, "Controller synthesis and clinical exploration of wearable gyroscopic actuators to support human balance," *Scientific Reports*, vol. 10, no. 1, p. 10 412, Jun. 2020.

[16] H. Schaub, S. R. Vadali, and J. L. Junkins, "Feedback control law for variable speed control moment gyros," *Journal of the Astronautical Sciences*, vol. 46, no. 3, pp. 307–328, 1998.

[17] D. Winter, *Biomechanics and motor control of human movement*. 2009.

[18] G. M. Espejel, "Using a friction model as engineering tool," *Evolution SKF*, vol. 6, no. 2, pp. 27–30, 2006.

[19] J. Braun, *Formulae Handbook*, 2020. [Online]. Available: http://support.maxongroup.com/hc/articles/360001900933 (visited on 12/30/2020).

[20] S. Derammelaere, M. Haemers, S. d. Viaene, F. Verbelen, and K. Stockman, "A quantitative comparison between BLDC, PMSM, brushed DC and stepping motor technologies," *2016 19th International Conference on Electrical Machines and Systems (ICEMS)*, p. 5, 2016.

[21] A. Gaude and V. Lappas, "Design and Structural Analysis of a Control Moment Gyroscope (CMG) Actuator for CubeSats," *Aerospace*, vol. 7, no. 5, p. 55, May 2020.

[22] P. T. Chinimilli, S. M. Rezayat Sorkhabadi, and W. Zhang, "Assessment of human dynamic gait stability with a lower extremity assistive device," *IEEE Engineering in Medicine and Biology Society*, vol. 28, no. 3, pp. 669–678, 2020.

[23] C. Buesing, G. Fisch, M. O'Donnell, I. Shahidi, L. Thomas, C. K. Mummidisetty, K. J. Williams, H. Takahashi, W. Z. Rymer, and A Jayaraman, "Effects of a wearable exoskeleton stride management assist system (SMA®) on spatiotemporal gait characteristics in individuals after stroke: A randomized controlled trial," *Journal of NeuroEngineering and Rehabilitation*, vol. 12, no. 1, p. 69, Dec. 2015.

[24] L. Valk, A Berry, and H. Vallery, "Directional Singularity Escape and Avoidance for Single-Gimbal Control Moment Gyroscopes," *Journal of Guidance, Control, and Dynamics*, pp. 1–14, 2018.

[25] S. Jabeen, A. Berry, T. Geijtenbeek, J. Harlaar, and H. Vallery, "Assisting gait with free moments or joint moments on the swing leg," in *2019 IEEE 16th International Conference on Rehabilitation Robotics (ICORR)*, Jun. 2019, pp. 1079–1084.

[26] M. Finn-Henry, A. Baimyshev, and M. Goldfarb, "Feasibility Study of a Fall Prevention Cold Gas Thruster," in *2020 8th IEEE RAS/EMBS International Conference for Biomedical Robotics and Biomechatronics (BioRob)*, Nov. 2020, pp. 611–616.

[27] C. Meijneke, B. Sterke, G. Hermans, W. Gregoor, H. Vallery, and D. Lemus, "Supplementary data for Design and Evaluation of Pint-Sized Gyroscopic Actuators," May 2021, Publisher: 4TU.ResearchData type: dataset. DOI: 10.4121/14578947. [Online]. Available: https://data.4tu.nl/articles/dataset/Design_and_Evaluation_of_Pint-Sized_Gyroscopic_Actuators/14578947.